Electrochemical behaviour of Alloy 600 tubing in thiosulphate solution

M.G. Faichuk [a,b,*], S. Ramamurthy [b], W.M. Lau [a,b]

[a] *Department of Chemistry, The University of Western Ontario, London, Ontario, Canada*
[b] *Surface Science Western, The University of Western Ontario, London, Ontario, Canada*

A R T I C L E   I N F O

A B S T R A C T

Electrochemical and surface properties of passive films formed on Alloy 600 in a thiosulphate solution were studied. Oxide films formed at various passive potentials contained a bilayer oxide, whose composition changed as a function of the applied potential resulting in a change in the impedance behaviour. Destabilisation of the oxide film at potentials within the passive region was observed, which was due to the breakdown of the oxide film and coincided with the loss of Cr within the passive film. In contrast, a higher degree of corrosion protection was obtained when the Cr content within the oxide film was elevated.

1. Introduction

Stress corrosion cracking (SCC) is the result of simultaneous exposure of a susceptible material to a corrosive environment and residual or applied tensile stress, resulting in localised fracture [1]. This type of corrosion can be severe, as catastrophic damage can occur even though the stress levels are within the specified range for normal operating conditions [1]. In CANDU™ nuclear reactors, the function of steam generator (SG) tubing is to contain and separate the primary and secondary water circuits, as well as to transfer heat from the primary water to the secondary water. The operating conditions of the tubing demand that it withstand temperatures, which together with manufacturing and formation residual stress can lead to SCC. Alloy 600 used to be one of the "superalloys" for fabricating SG tubing, but numerous failures over the years have detailed underlying issues with Alloy 600 SG tubing, and it is now well-known to be susceptible to pitting corrosion and SCC [2–5]. SCC of SG tubing can result in the contamination of secondary water with highly radioactive primary water. Thus, there is strong incentive to better understand this type of corrosion and methods for its prevention.

Many publications have detailed the corrosion behaviour of Alloy 600 in a variety of aqueous solutions: sodium sulphate (Na_2SO_4) [6–8], sodium hydroxide (NaOH) [9], sodium thiosulphate ($Na_2S_2O_3$) [10], and boric acid (H_3BO_3) [11]. $Na_2S_2O_3$ was of particular interest, as polarisation curves of oxide films grown in thiosulphate solutions showed regions of increased current density within the passive region, a feature not observed in Na_2SO_4 or H_3BO_3 solutions. This behaviour was also observed, but to a much lesser extent on the current alloy of choice, Alloy 690 [12]. Little is known about the structure or behaviour of the passive film formed in $Na_2S_2O_3$, and it is still unclear what transpires on the surface of the alloy or why corrosion enhancement of Alloy 600 is observed at certain potentials. This is an important issue given Alloy 600's susceptibility to SCC in this solution [13–16]. The aim of this study is to examine the surface composition of the oxide film formed in the passive region at various potentials in $Na_2S_2O_3$ using Auger electron spectroscopy (AES) and X-ray photoelectron spectroscopy (XPS), and to determine the corrosion behaviour at these potentials using electrochemical impedance spectroscopy (EIS).

2. Experimental details

9.5 mm diameter Alloy 600 tubing sections were procured from Rolled Alloys Canada in the mill-annealed condition from heat number 123154. The composition of this alloy is presented in Table 1. Small rectangular prismatic coupons were cut from this tubing using a Buehler diamond-tipped saw. The average area on the outer surface of these coupons was 20 mm². The coupons were extensively polished, finishing with a 0.05 μm alumina grit polishing pad and washed with deionized water and sonicated in acetone.

Electrochemical measurements were carried out using the sample coupons. Electrodes were assembled by spot welding a stainless steel wire onto the polished coupon. The back and sides of the coupon, as well as the wire, were coated with a microsheild™ masking aid. A solution of 0.1 M $Na_2S_2O_3$ was used for the

* Corresponding author at: Department of Chemistry, The University of Western Ontario, London, Ontario, Canada.

E-mail address: mfaichuk@uwo.ca (M.G. Faichuk).

Table 1
Chemical composition of Alloy 600 steam generator (SG) tubing (wt%).

Ni	Cr	Fe	Mn	Al	Ti	Si	Co	C	P	S
Bal.	16.14	9.65	0.34	0.27	0.23	0.11	0.08	0.03	0.007	0.001

electrochemical experiments and was made using deionized water with a resistivity of 18.2 MΩ cm. The $Na_2S_2O_3$ solution had a room temperature pH of approximately 6.5. The three-electrode cell consisted of a platinum foil counter electrode, a saturated calomel reference electrode (0.2412 V vs. SHE), and the Alloy 600 coupon acting as the working electrode. To purge the system of oxygen, argon gas was vigorously bubbled through for 30 min. A steady flow of argon gas through the solution was maintained for the duration of the experiment. At the beginning of each experiment, a reducing potential of $-1.2 V_{SCE}$ was applied for 1 h. Potentiodynamic polarisation experiments were run using a Solartron 1286 potentiostat (scan rate 0.167 mV/s). The experiments were started $0.150 V_{SCE}$ below the measured open circuit potential and were terminated at $1 V_{SCE}$.

Using the same preparation technique, analysis of the samples was conducted using electrochemical impedance spectroscopy (EIS), which allows for the in-depth analysis of the electrochemical behaviour of the oxide film formed on the sample surface. In these impedance measurements, a sinusoidal potential perturbation was applied to the sample electrode and the resistive and capacitive responses determined the current response magnitude and phase shifts. The cell set-up remained unchanged, and pre-treatment measures included cathodic cleaning at $-1.2 V_{SCE}$ for 1 h, followed by exposure to an applied potential for 8 h. Potentials selected for analysis were determined based on the anodic polarisation curve. The frequency range was between 65 kHz and 0.01 Hz, with measurements made using a Solartron 1250 frequency response analyser. The data was collected and modelled using ZPlot™ and ZView™ software, respectively.

Auger data was obtained using a PHI 660 Auger electron spectroscopy (AES) instrument with an excitation energy of 5 keV. An Ar^+ ion beam was used for sputtering to obtain depth profile measurements. In order to ensure proper conductivity, the masking agent was stripped from the sample and the wire, which had been previously spot wielded onto the sample, was removed in order to fit into the coupon into the sample holder. For each sample, a survey scan was acquired, and during depth profiling the intensity for elements such as Ni, Cr, Fe, C, and O was monitored as a function of sputter time. Sputter time profiles were converted into concentration using a sputter rate of 7.6 nm/min, which was determined by the depth profiling of a reference sample under the same conditions.

X-ray photoelectron spectroscopy (XPS) analyses were conducted on the sample electrodes after exposure to the $Na_2S_2O_3$ solution at various potentials. Immediately following treatment, samples were rinsed with DI water and methanol. A Kratos AXIS Ultra spectrometer was employed for analysis using a monochromatic Al Kα electron source (15 mA, 14 kV). To calibrate the work function of the instrument, the binding energy (BE) for the Au $4f_{7/2}$ line was set to 83.96 eV and the spectrometer dispersion was adjusted using Cu $2p_{3/2}$, whose BE was 932.62 eV. The instrument base pressure was held at approximately 2.5 e^{-7} Pa. For each sample, survey scan analyses were carried out over an area of 256×256 μm at a pass energy of 160 eV between 0 and 1000 eV. High resolution scans of Ni $2p_{3/2}$, Cr $2p_{3/2}$, C 1s and O 1s peaks were obtained at a pass energy of 20 eV from the same area with a step size of 0.05 eV. The windows for these elements were (890–847 eV), (595–570 eV), (540–525 eV), and (295–278 eV), respectively. Spectral analysis was performed using CasaXPS™ software.

With the exception of Cr $2p_{3/2}$, all spectra have been charge corrected to the main line of the C 1s spectrum.

3. Results and discussion

3.1. Electrochemical behaviour of Alloy 600 in 0.1 M $Na_2S_2O_3$

The potentiodynamic response of Alloy 600 in de-aerated 0.1 M $Na_2S_2O_3$ solution is shown in Fig. 1. The graph displays a modified S-shape curve, indicative of active–passive–transpassive behaviour [8,10,12,17]. The open circuit potential for this alloy was $-0.45 V_{SCE}$ and the passive region, which can be characterised by a steady state current density over a variable potential range, lies between -0.40 and $0.88 V_{SCE}$. Within this region two anodic peaks were clearly identified at 0.10 and $0.75 V_{SCE}$. Their presence corresponds well with previously reported values [10,12,15,17]. Work by Congleton and co-workers have shown that the addition of $Na_2S_2O_3$ to solution destabilizes the oxide film, creating more anodic peaks [18]. The instability of this alloy in the presence of thiosulphate is believed to be caused by an enhanced ability to promote anodic dissolution and impede repassivation [19,20]. It has also been previously reported that the active–passive behaviour of Alloy 600 is heavily influenced by Cr [6,15,21]. Therefore, it is possible that the removal of Cr could be responsible for the changes in current density observed [6]. Based on the anodic polarisation curve, three separate regions were established; pre-passive, passive I and passive II. The pre-passive region was located between -0.6 and $-0.45 V_{SCE}$, while passive region I encompassed a range between -0.45 and $0.2 V_{SCE}$ to include the first anodic peak. Passive region II included the second anodic peak, and was between 0.2 and $0.8 V_{SCE}$. The division between the two passive regions was based on the rapid increase in current density with increasing potential beyond $0.2 V_{SCE}$. Oxide films were electrochemically grown on the alloy surface at -0.6, -0.4, -0.2, 0, 0.1, 0.2, 0.4, 0.6, and $0.75 V_{SCE}$.

The electrochemical properties of the oxidised species on the surface of the alloy were measured using impedance spectroscopy. Fig. 2 shows the Nyquist plot for the experimental and fitted data at a potential in each of the three regions. For each spectrum, the semi-circles were incomplete. As the polarisation applied to the electrode became more anodic, the semi-circles appeared to be more depressed. The measured impedance was the largest for
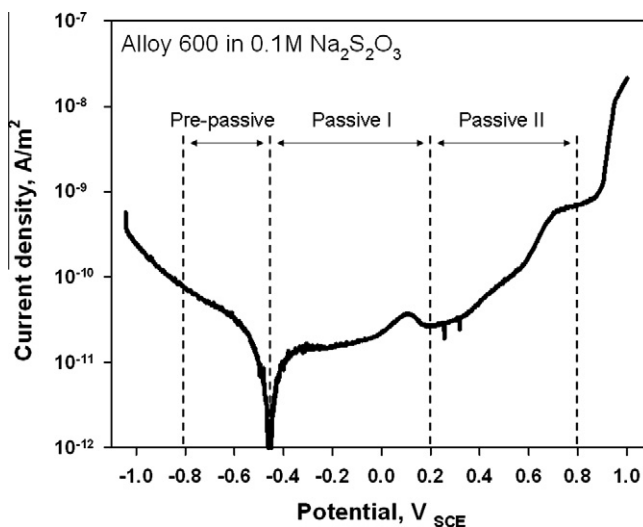
Fig. 1. Anodic polarisation curve for Alloy 600 in 0.1 M sodium thiosulphate solution. The curve is divided into three regions: Pre-passive (-0.6 to $-0.4 V_{SCE}$), passive 1 (-0.4 to $0.4 V_{SCE}$) and passive 2 ($0.4–0.75 V_{SCE}$).
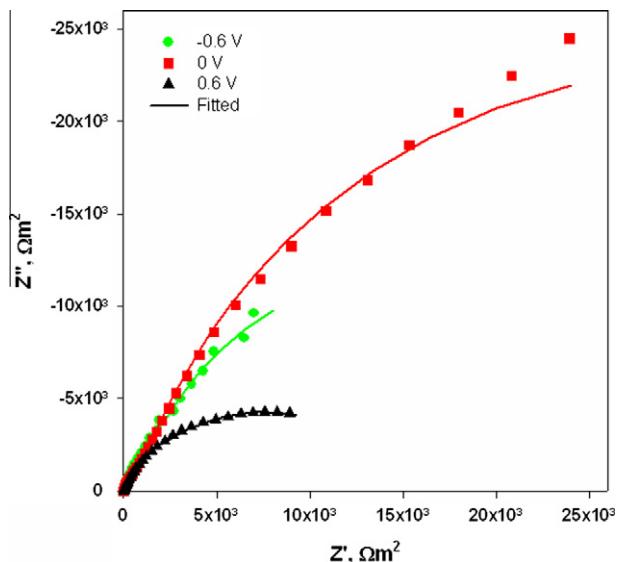
Fig. 2. Nyquist plots for the experimental and fitted data for Alloy 600 at −0.6, 0 and 0.6 V_{SCE}.

the potential in the first passive region (0 V_{SCE}), while the impedance in the second passive region (0.6 V_{SCE}) was significantly lower. All of the Nyquist plots exhibit features that suggest the presence of a rough or porous surface. Typically in cases such as this, the measured capacitance response is not ideal, and a modification can be applied. When creating a model that will accurately represent the acquired data, a constant phase element (CPE) can be used and the CPE can account for the surface inhomogeneities. The impedance of a CPE is given by Eq. (1) [22].

$$Z_{CPE} = 1/Q(j\omega)^{\alpha} \tag{1}$$

In this equation, Q is a fit parameter that is independent of frequency and exponent α has a value between 0 and 1. For example, if $\alpha = 1$, then Q can be taken as equal to capacitance C. Fig. 3 presents the bode plots at applied potentials of (a) −0.6 V_{SCE}, (b) 0 V_{SCE} and (c) 0.6 V_{SCE}. In all three regions, the phase angle portion of the bode plot contained two peaks, although these were most easily resolved at 0 V_{SCE}. At lower frequencies, the phase angle decreased as the potential, starting in the pre-passive region, was moved through to the passive II region. Fitting of the impedance data was accomplished using the equivalent circuit shown in Fig. 4, which has been applied in similar systems [6,8,23–25]. This circuit contains a resistor to account for the solution resistance, which is in series with two time constants, R_1/CPE$_1$ and R_2/CPE$_2$. These time constants take into account the properties of the outer (1) and inner (2) oxide layer. Plots of the inner and outer resistance values as a function of potential are shown in Fig. 5. It is interesting to note that within the passive I region, the resistance of the inner oxide overwhelmingly dominates, exceeding the values of the outer resistance by more than an order of magnitude. After peaking at −0.2 V_{SCE}, the values recorded for the inner resistance begin to decrease. In the passive II region, the resistance of the outer oxide layer nearly doubles, while the inner oxide resistance continues to drop to levels below those observed in the pre-passive region.

The CPE parameters obtained can be converted into true capacitance values using Eq. (2) [26,27].

$$C_{eff} = Q(\omega_{max})^{\alpha-1} \tag{2}$$

C_{eff} can be calculated by taking the CPE parameter (Q), the exponent (α) and the frequency at which the magnitude of the imaginary component of the impedance reaches a maximum for the
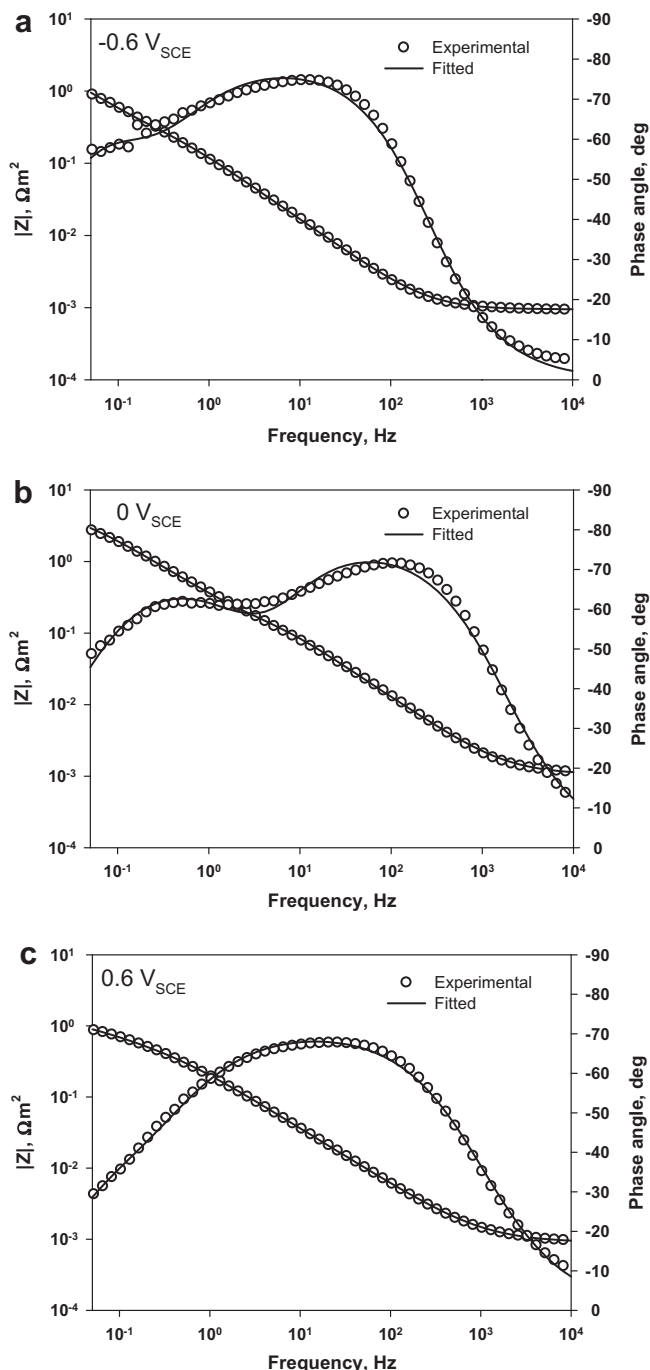

Fig. 3. Bode plots of the experimental and fitted data for Alloy 600 at (a) −0.6 V_{SCE}, (b) 0 V_{SCE} and (c) 0.6 V_{SCE}.
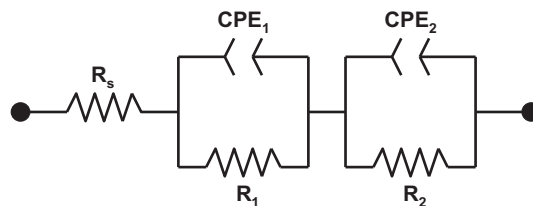

Fig. 4. Equivalent circuit for the bilayer oxide film on Alloy 600 in 0.1 M Na$_2$S$_2$O$_3$ solution containing a solution resistance, R_s, and two time constants (R_1/CPE$_1$ and R_2/CPE$_2$) in series representing (1) the outer oxide layer and (2) the inner oxide layer.
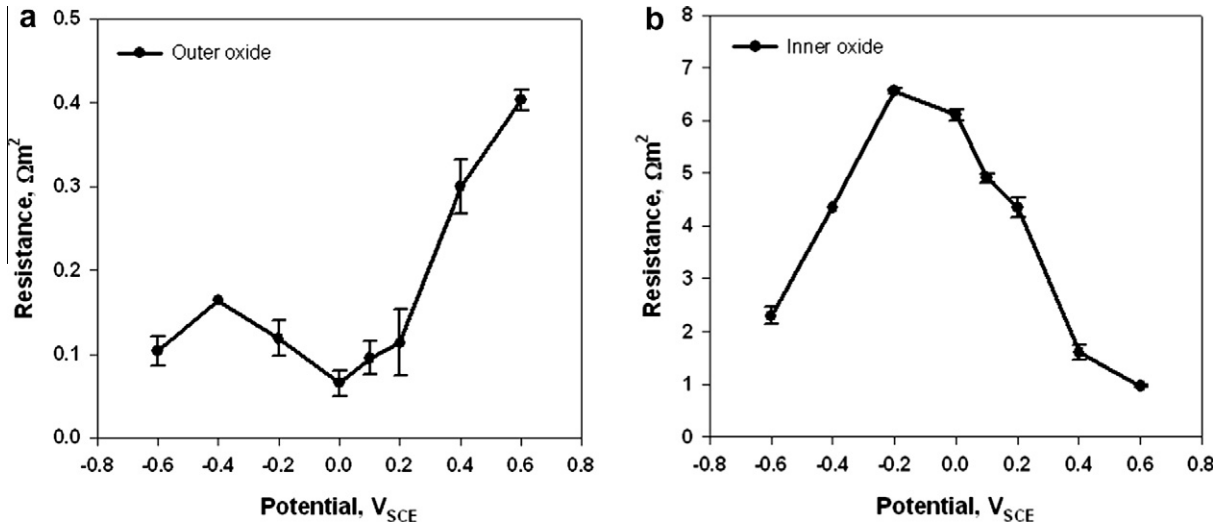
Fig. 5. Resistance values of the (a) outer (R_1) and (b) inner (R_2) oxide films as a function of applied potential.

time constant in question (ω_{max}). The effective capacitance can then be used to examine the thickness of the oxide film using Eq. (3) [25].

$$C = \varepsilon\varepsilon_0(A/d) \qquad (3)$$

Knowing the area of analysis, *A*, the inverse of the capacitance allows for an estimation of the oxide film thickness, *d*. Fig. 6 shows the inverse capacitance plotted for the inner and outer oxide layer. This plot suggests that the outer oxide film is much thicker than the inner barrier layer. Further details regarding this data will be discussed later.

3.2. Surface analysis of bilayer oxide film – AES

In order to determine the film thickness, it was essential to first establish the position of the oxide/alloy interface. Due to ion beam mixing, this interface is difficult to establish, so approximations must be made. Methods developed by Sato and co-worker allowed for the estimation of the interface position through extrapolation of the oxygen peak [28], however a more simplistic approach was taken. Oxide film thickness was determined to be approxi-
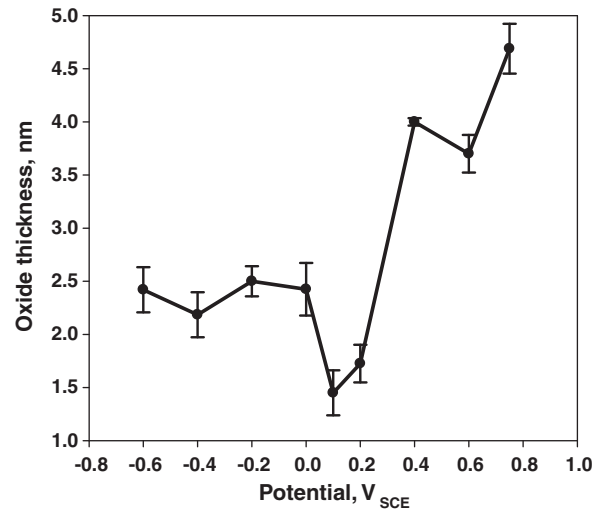

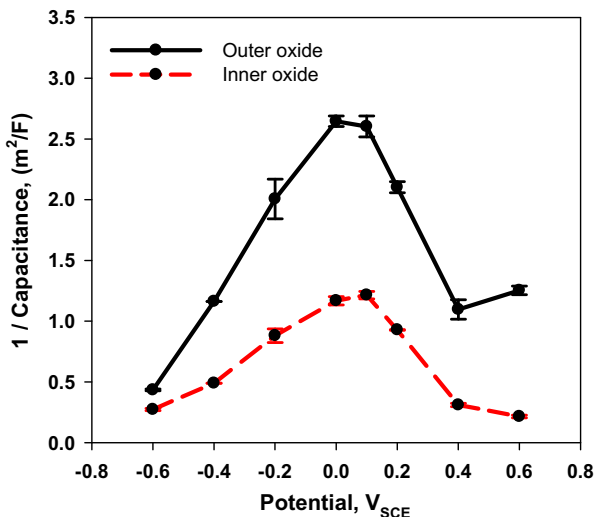**Fig. 7.** Oxide film thickness calculated from the AES depth profile oxygen peak.

mately the depth at which the oxygen concentration reaches 50% of its maximum value [29–31]. From the plot in Fig. 7, the change in oxide thickness as a function of applied potential showed that the growth of the oxide film increased with increasing potential, which is in agreement with studies conducted previously [28,32]. Upon passivation of the alloy surface at -0.4 V_{SCE}, the oxide thickness began to increase. This film growth was interrupted at 0.1 V_{SCE}, but resumed upon re-passivation at 0.2 V_{SCE}. This data again shows that the removal of the oxide film corresponded to the first anodic peak observed in the polarisation curve. The increase in film thickness between passive regions I and II was substantially greater than at any other measured potential. There was no significant change between 0.4 and 0.6 V_{SCE}, but at the second anodic peak (0.75 V_{SCE}) another increase in thickness was observed.

Previously published data has shown that oxide films formed on similar alloys develop into a bilayer oxide with a Cr-rich barrier (inner) layer and an outer layer containing a mixture of Ni and Fe [6,11,21,33–35]. Fig. 8(a) through (c) shows the AES depth profile at three different potentials and the composition of the oxide double layer that was observed on each sample. Subtle changes to the oxide composition can be visualised by plotting the cationic
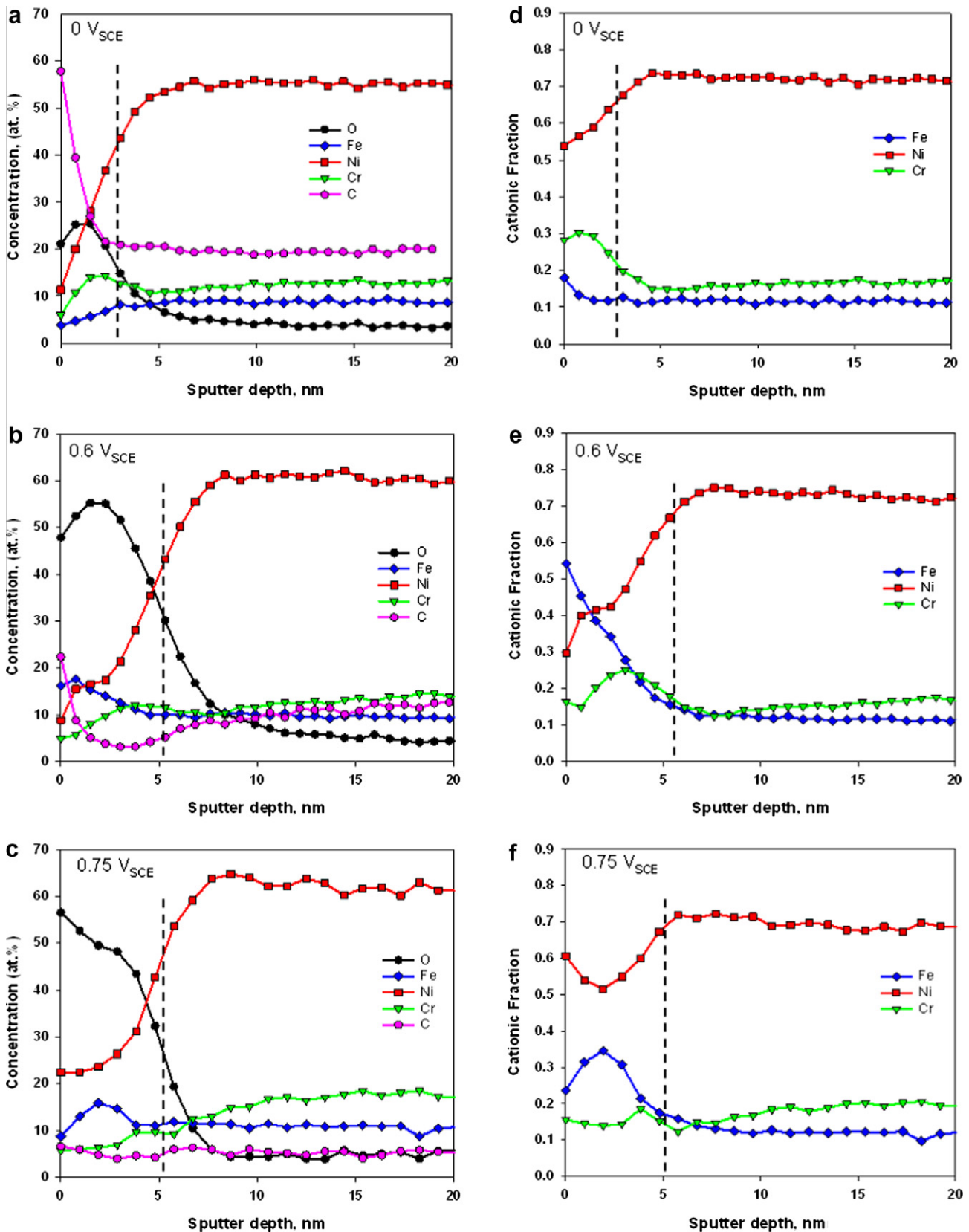

Fig. 6. Inverse capacitance of the inner and outer oxide layer as a function of potential.

Fig. 8. AES depth profiles at (a) 0 V_{SCE}, (b) 0.6 V_{SCE} and (c) 0.75 V_{SCE} and Alloy 600 AES cationic fractions at (d) 0 V_{SCE}, (e) 0.6 V_{SCE} and (f) 0.75 V_{SCE}. The cationic fractions were calculated by dividing Ni, Fe or Cr by the sum (Ni + Fe + Cr).

fractions, which were obtained by taking the concentration of the individual alloying element (Ni, Cr or Fe) and dividing it by the total concentration of the three alloying elements (Ni + Cr + Fe). Using this methodology, changes that may have gone unnoticed

previously, such as the enrichment of Fe at 0 V_{SCE} in Fig. 8(d), could be clearly observed. These plots also aid in amplifying other compositional changes, such as the enrichment and depletion of Cr and Ni in Fig. 8(e) and (f). Although not shown, plots of the potentials between −0.6 and 0.2 V_{SCE} had a very similar appearance to the plot at 0 V_{SCE}. Only subtle changes, such as a gradual decrease in Ni, as well as minor fluctuations in Cr were identified. In the second passive range, a more substantial increase in Fe was observed, as well as a depletion of Cr on the outer surface. Changes in the Ni profile were also evident. Although Ni was observed to have to been removed from the surface in the beginning of the second passive region, the profile obtained at 0.75 V_{SCE} in Fig. 8(f) shows that Ni once again precipitated back onto the surface. In addition to the changes observed in the oxide film, it is interesting to note that a metallic layer can be found directly below the oxide and is distinguishable from the bulk composition. Differences can be seen in Fig. 8(d) and (f), at potentials of 0.6 and 0.75 V_{SCE}. In both cases, this metallic layer appears to be deficient in Cr. Only at a depth of approximately 10 nm is the bulk composition finally measured. At lower potentials, the depletion of Cr within the metallic layer was not as severe.

In order to more effectively track the changes in film composition, the cationic fractions for Ni, Fe and Cr were plotted along the measured potential range in Fig. 9. To account for the changes occurring in both layers, values for the outer oxide were taken where the maximum oxygen value was observed, while values for the inner oxide were taken at the oxide/metal interface, defined as the depth at which 50% of maximum oxygen concentration is reached. Fig. 9(a) shows the cationic fractions of Ni as a function of applied potential for the inner and outer oxide layers. Compared to the outer layer, the changes in the inner layer were insignificant, which is consistent with the observation that Ni should only be present within the outer oxide layer in any significant amount. The concentration of Ni within the outer layer was shown to decrease as the potential increased, with the disparity between the two layers becoming more apparent upon entering passive region II. At potentials of 0.1 and 0.75 V_{SCE}, a statistically significant spike in the Ni content was observed, which corresponded to the rise in current density on the anodic polarisation curve. The cationic fraction for Fe in Fig. 9(b) revealed strikingly similar but inverse behaviour when compared to Ni. Within the pre-passive and passive I region, the majority of Fe was located on the outer surface of the oxide film. Beyond 0.2 V_{SCE}, the disparity between the Fe concentration within the inner and outer layer was amplified. At 0.75 V_{SCE}, a drop in Fe concentration was observed. Based on these results, it appears that the rise in current density at the anodic peaks was due to the removal of Cr (0.1 V_{SCE}) and Fe (0.75 V_{SCE}), and the subsequent accumulation of Ni at both potentials.

According to numerous authors, the critical Cr concentration required to develop a protective Cr oxide layer is approximately 15% [36]. It has been demonstrated that at Cr concentrations greater than 10–15% the behaviour of the alloy will begin to resemble that of pure Cr [6,21] and it is for this reason that the Cr rich inner oxide layer is believed to be vital to the corrosion resistant behaviour of this alloy. A significant portion of Cr was located within the outer layer, though the exact position is uncertain with this technique. Upon passivation of the metal at −0.4 V_{SCE}, the Cr concentration in the film increased. While some minor fluctuations in concentration were observed at various potentials in the first passive region, a significant drop was noted at 0.1 V_{SCE}, corresponding to the first anodic peak. Upon re-passivation of the film at 0.2 V_{SCE}, the Cr content returned to a value similar to those preceding the film breakdown. In the second passive region, a substantial drop of Cr content in the outer layer was observed, though no significant changes occurred in the inner layer.
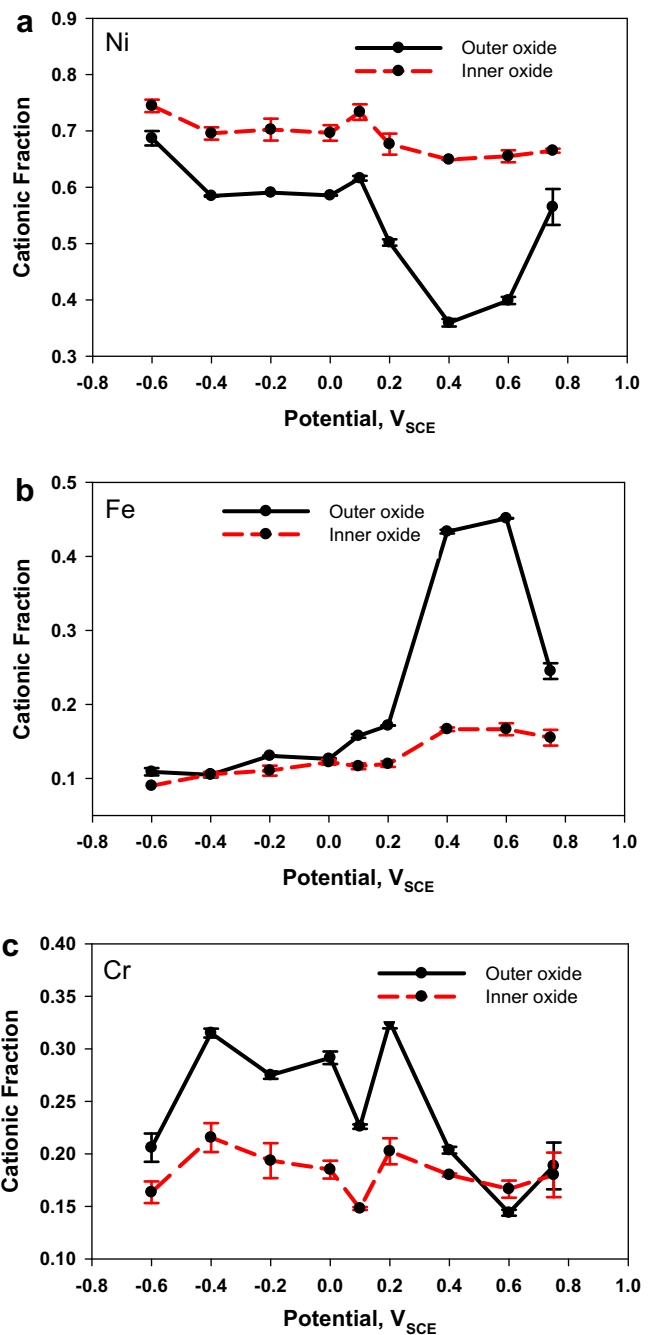

Fig. 9. Cationic fraction plotted as a function of applied potential for (a) Ni, (b) Fe and (c) Cr.

Cr/Ni ratios at various applied potentials can provide an indication of the degree of enrichment of either Ni or Cr in the oxide layer. Using the Auger data, these ratios were calculated for the inner and outer layers and are shown in Fig. 10. In both layers, Cr enrichment was clearly observed at −0.4 V_{SCE}, when the passive oxide film forms. The first indication of Cr depletion was observed at 0.1 V_{SCE}, where the anodic peak suggested film breakdown. When the film recovered at 0.2 V_{SCE}, Cr enrichment was again observed. This enrichment was maintained within the inner layer throughout both passive regions. The outer layer, on the other hand, experienced significant depletion of Cr when it entered the second passive region. This data correlates very well with the cationic fractions plotted as a function of potential.
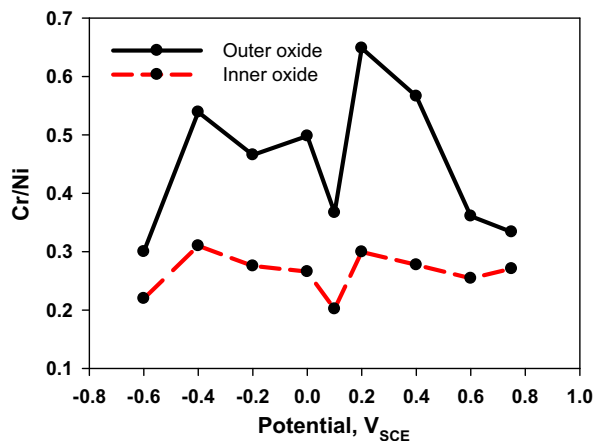
Fig. 10. Cr/Ni ratios for the inner and outer oxide layer obtained from AES analysis plotted as a function of potential.

3.3. Surface analysis of bilayer oxide film – XPS

The composition of the oxide film at various applied potentials was also studied using XPS because of its ability to identify the chemical state of the elements of interest. Following electrochemical treatment, samples were introduced into the vacuum chamber for analysis without sputtering. Spectra and fitting of the high resolution Ni $2p_{3/2}$, Cr $2p_{3/2}$ and O 1s on Alloy 600 at 0 V_{SCE} are shown in Fig. 11. The XPS signals for Cr $2p_{3/2}$ were fitted according to the contributions made by the different chemical states [37,38]. At least three different chemical forms of Cr were found on the sample surface, namely metallic Cr at 574.1 eV, a Cr oxide species (Cr_2O_3) at 575.8 eV and a Cr hydroxide species ($Cr(OH)_3$/CrOOH) at 577.3 eV. The FWHM values for these peaks were 1.00, 1.10 and 2.50, respectively. Although only one peak for Cr^{3+} was observed in the spectra, it was determined that both the oxide and hydroxide were required to achieve an adequate fit. Attempts to fit either component individually produced binding energies that were exceptionally deviant from reported literature values. Our references, along with the peak fitting procedures developed over a number of years show that the Cr(III) oxide species will show a discrete structure containing five peaks that is indicative of multiplet splitting. Binding energies for both the oxide and hydroxide components were within 0.2 eV of the reported literature values, with Cr metal at 574.2 eV, Cr_2O_3 at 575.7 eV and $Cr(OH)_3$ at 577.1 eV. [37,38]. These binding energies suggest that both the Cr oxide and hydroxide are in close proximity to the metal surface. According to a previous study, the Cr hydroxide will overlay the oxide component [38]. Similar to Cr $2p_{3/2}$, the Ni $2p_{3/2}$ spectra also suggests the presence of three different chemical species. Ni metal was detected at 852.53 eV, a Ni oxide species (NiO) at 853.45 eV, and a Ni hydroxide species ($Ni(OH)_2$) at 855.46 eV (with a satellite at +5.7 eV with respect to the main signal). The FWHM values for these peaks were 0.94, 1.02 and 1.10, respectively. Both the Ni metal and oxide peaks were within 0.2 eV of reported literature values, with Ni metal at 852.6 eV and NiO at 853.7 eV [39]. The binding energy for $Ni(OH)_2$, which had a reported literature value of 854.9 eV, was strongly shifted due to preferential charging of the species, resulting from the $Ni(OH)_2$ forming on the outer surface, furthest away from the metal alloy. As was the case with Cr, the Ni metal peak was also present. The presence of both Ni and Cr metal indicates that the oxide film is very thin. Previous reports have shown Ni metal to be present within the oxide, which would explain the observation of a stronger signal intensity compared to the Cr metal. [6,28,31,40]. The O 1s spectrum contained three different components as well. The first peak at 529.93 eV was charac-

Fig. 11. High resolution XPS fitting for (a) Cr, (b) Ni and (c) O. The dashed line shows the original data, and the solid line show the fitted data.

teristic of an anhydrous oxide species, M–O (M being the alloy), while the second peak at 531.59 eV was a result of the hydrated oxide species, M–OH. The final peak was due to residual water
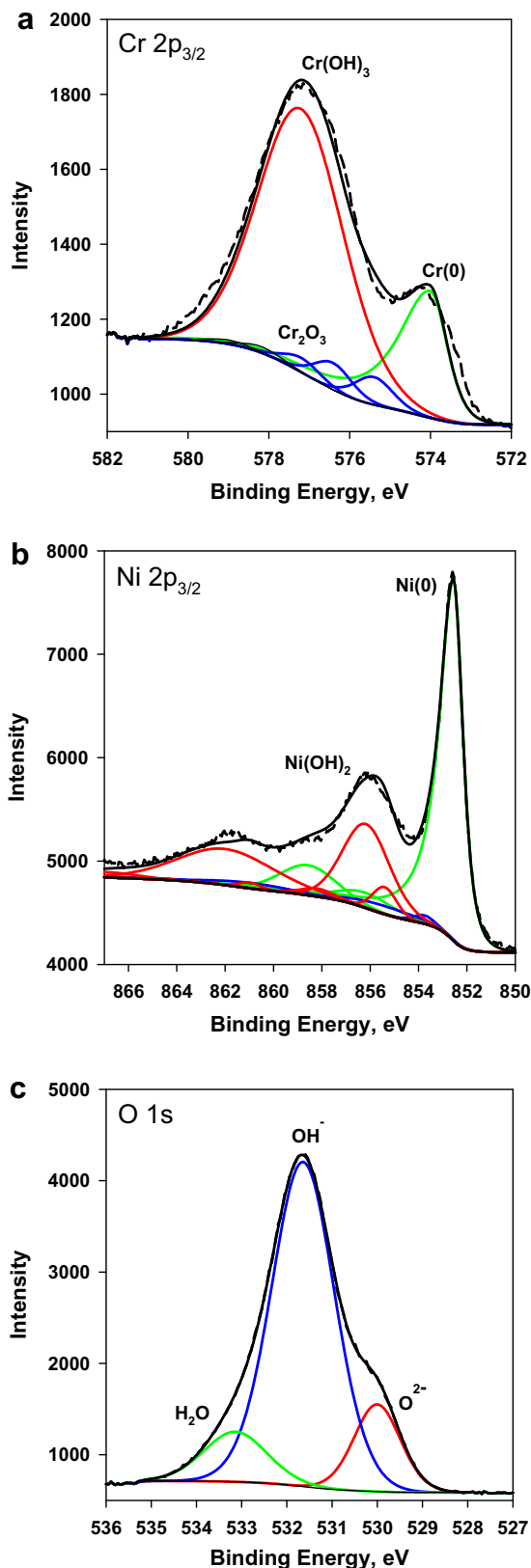
on the sample surface. All species were present in various amounts throughout the measured potential range and were within 0.2 eV from recorded literature values [36]. Fe was not included in this analysis due to the overlap of the Fe 2p peak with the Ni KLL peak, making it difficult to obtain any meaningful results.

The changes in the individual Cr components as a function of potential are shown in Fig. 12(a). To determine the concentration (atomic percent), the contributions of each fitted component were normalised to the percent composition of that particular element present on the sample surface during the survey scan. Within the pre-passive and passive I region, the majority of Cr was present
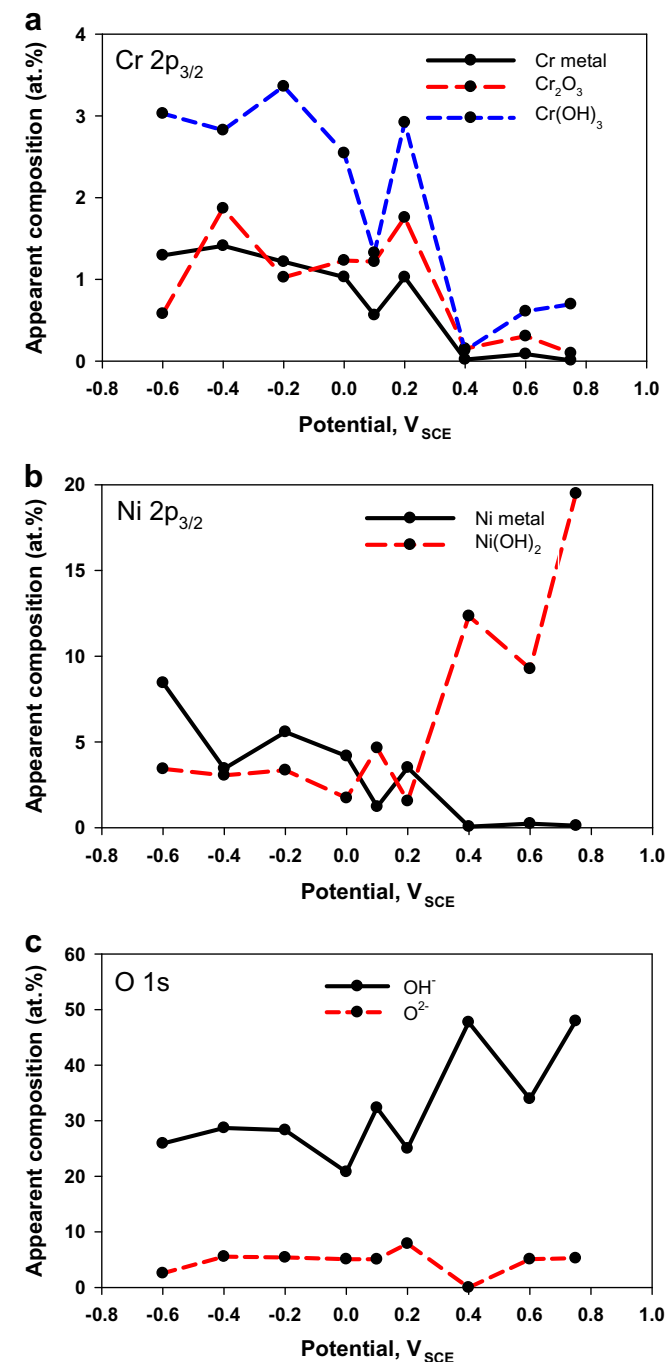
Fig. 12. XPS high resolution components as a function of potential of (a) Cr, (b) Ni and (c) O. Values were normalised based on the composition% of the survey scan.

as $Cr(OH)_3$ and the concentration remained high, with some minor fluctuations until 0.1 V_{SCE}. It became clear from Fig. 12(a) that the preferential dissolution of the film at 0.1 V_{SCE} was due to the removal of $Cr(OH)_3$. Cr_2O_3, on the other hand, was present in very small quantities in the pre-passive region. At -0.4 V_{SCE} the Cr oxide content increased, coinciding with the formation of the oxide film. While exhibiting some fluctuations in concentration, these values remained elevated for the entirety of passive region I. Unlike $Cr(OH)_3$, Cr_2O_3 did not show any change that correlated with the anodic peak at 0.1 V_{SCE}. When the potential reached 0.4 V_{SCE}, all measured forms of Cr had decreased to values approaching zero. At higher potentials the metal and oxide components remained extremely low, though small amounts of $Cr(OH)_3$ were detected within the oxide film. High resolution XPS data for Ni presented in Fig. 11(b) displayed a particularly intense Ni metal peak at -0.6 V_{SCE}, which decreased as the potential became increasingly anodic. The metal peak remained as the dominant feature until 0.1 V_{SCE}, at which point the hydroxide component surpassed the metal component. At 0.4 V_{SCE}, there was another spike in the hydroxide while virtually no trace of the metal was observed. It is interesting to note that at both 0.1 and 0.4 V_{SCE} the spike in $Ni(OH)_2$ always coincided with a decrease in $Cr(OH)_3$. Any contributions made from NiO throughout the potential range were so close to 0, they were considered negligible. The O 1s plot in Fig. 12(c) indicated that hydroxide was the primary component of the oxide film, while the lattice oxide made up a significantly smaller portion. Substantial increases in the hydroxide were observed at both 0.1 and 0.4 V_{SCE}. Since the majority of Alloy 600 is composed of Ni, it is reasonable to assume that a substantial amount of the hydroxide in the O 1s spectrum is due to the $Ni(OH)_2$ component of the Ni $2p_{3/2}$ spectrum. The presence of the metal peak for both Ni and Cr in the pre-passive and passive I region suggests that the oxide films were below the depth of analysis in XPS, which is $\sim$6 nm, based on the calculation from the inelastic mean free paths of Ni and Cr. In the second passive region, the metal components were observed in much smaller quantities, indicating that the oxide film had, or was very close to surpassing the observable depth dictated by the inelastic mean free path of these two elements. Similar to the AES oxide depth results, the high resolution XPS data also suggests that the oxide film was thickening with increasing potential.

The chemical state of sulphur present on the oxide surface was also investigated using XPS. Since high-resolution data was not collected for this element, peak fitting was applied to the S 2p signal present in the survey scans. An example of this fitting is shown in Fig. 13(a) for Alloy 600 at a potential of 0.4 V_{SCE}. Two peaks were present in the S 2p spectra, one at a binding energy of approximately 168.4 eV (peak 1) and the other at 162.9 eV (peak 2) with an error of approximately 0.5 eV. Contributions to peak 1 were likely due to more oxidised sulphur species such as thiosulphate and sulphate components, while peak 2 could be due to more reduced sulphur species, such as thiosulphate as well as sulphide [41]. To track the changes in sulphur chemistry, the areas were recorded for the peaks and plotted as a ratio of peak 1/peak 2 as a function of the applied potential (Fig. 13(b)). This figure shows that the peak 1/peak 2 ratio remained around 0.2 at potentials up to -0.2 V_{SCE} and continually increased to 2.3 until 0.6 V_{SCE}. At potentials greater than 0 V_{SCE}, an increase in the current density was observed in Fig. 1 and this corresponded to an increase in peak 1/peak 2 ratios in Fig. 13(b). This indicates that sulphur species are becoming oxidised at higher applied potentials. However, no significant changes in peak 1/peak 2 ratios were observed at 0.1 and 0.75 V_{SCE}, potentials which correspond to the breakdown of the passive film as shown in Fig. 1. This suggests that sulphur species may not play a role in the breakdown of the passive film at these potentials.
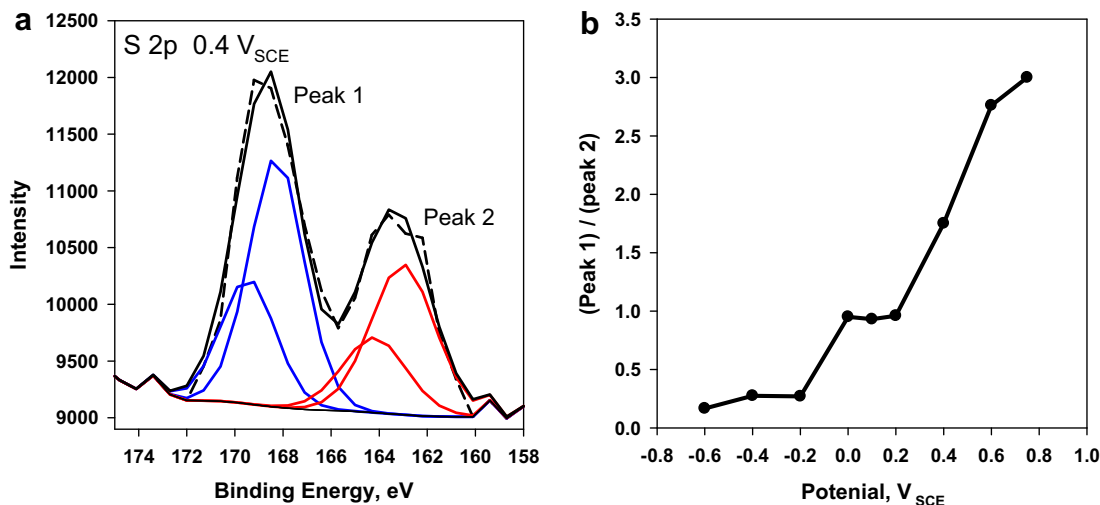
Fig. 13. (a) Fitted S 2p from the survey scan at 0.4 V_{SCE}. The dashed line shows the original data and the solid line shows the fitted data. (b) Plot of the ratio of peak 1/peak 2 as a function of potential.

3.4. Film growth through the point defect model

The results obtained in this study can be understood through application of the point defect model (PDM), which was developed and refined by Macdonald and co-workers [42–44] and has been adopted by many other authors [8,28,45]. This model, whose physiochemical processes are outlined in Fig. 14, was created to understand and describe the different reactions involved in the growth and dissolution of a passive bilayer film. For simplicity, only Cr is shown in the model. The outer oxide layer can be a porous mixture of both Ni and Fe hydroxides, whose formation occurs through the hydrolysis of cations ejected from the barrier layer and subsequently precipitate on the outer surface. Evidence has been gathered to support this theory, as alloying elements are often observed in both oxide layers while species in solution, such as those that make up the electrolyte, are only located in the outer layer [30]. The inner layer is primarily composed of a much thinner and more resistive anhydrous Cr oxide (Cr_2O_3). Fig. 14 shows the injection of the metal interstitial (1) into the barrier layer. It is

ejected into the solution (3) under the influence of an electric field. The annihilation of oxygen vacancies is shown by (4), while the growth of the barrier is represented by (2). The removal of the barrier layer is shown by (5) [45].

The variations in diffusion rates for Ni, Cr and Fe in Eq. (4) is viewed as one of the underlying causes for the different oxide layer compositions [36].

$$Fe^{2+} > Ni^{2+} \gg Cr^{3+} \tag{4}$$

Faster diffusing impurities, such as Fe and Ni, will pass through to the outer layer while slower diffusing impurities, such as Cr, will be oxidised without movement and remain in the barrier layer. A consequence of the varying diffusion speed is that the Cr ions retained in the barrier layer slow the diffusion of other ions, allowing the inner barrier layer to control the rate [31]. This model is supported exceptionally well by the data obtained in this study. The AES plots in Fig. 8 clearly show the double layer, with the enrichment of Fe and Ni at the surface and Cr below. Similar results were
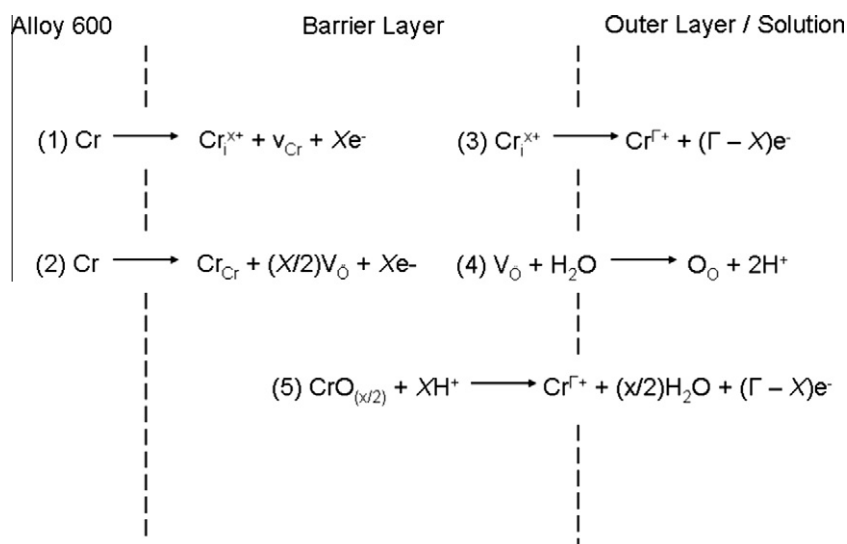

Fig. 14. Schematic for the point defect model: Cr: metal atom, Cr_{Cr}: metal cation on the metal sublattice of the barrier layer, Cr_i^{x+}: interstitial cation, V_{Cr}: cation vacancy on the metal sublattice of the barrier layer, $V_{\ddot{O}}$: oxygen vacancy on the oxygen sublattice of the barrier layer, O_O: oxygen anion on the oxygen sublattice of the barrier layer, $Cr^{\Gamma+}$: metal cation in solution [29].

obtained at the different measured potentials throughout the entire passive region. Through analysis of the XPS data, only a small portion of Cr was contained in the barrier layer as Cr_2O_3, while the majority was discovered in the hydroxide form. Both the AES depth profile and cationic fraction plots show the Cr peak maximum occurring at an intermediate point between the outer surface and the oxide/metal interface. A schematic for the layering of the oxide film at different potential regions is shown in Fig. 15. For simplicity, this model only takes into account the passive oxide film and not the metallic layer directly underneath the oxide. A similar structure was observed for Alloy 600 at high temperatures [46]. These results vary somewhat from the point defect model put forth with the presence of $Cr(OH)_3$ overlaying the Cr_2O_3. Experiments have found that these elements do not always follow the diffusion patterns outlined above as Ni, Cr and Fe are often dispersed throughout the entire oxide [6]. It is possible that not all of the Cr was utilised in creating the barrier layer and that some diffused out into solution, only to precipitate back onto the surface.

Because the film composition was observed to change as a function of applied potential, it was unsurprising that the film thickness also varied. Growth of the oxide film was observed once passivation had been established at -0.4 V_{SCE}. The formation of this passive film was accompanied by an increase in Cr, as observed through Auger analysis, and was identified as Cr_2O_3 through high resolution XPS. Within the passive region, the oxide thickness increased with applied potential. A drop in film thickness was observed at 0.1 V_{SCE} and surface analysis revealed substantial compositional changes. The film breakdown resulted from a loss of $Cr(OH)_3$. Interestingly, $Ni(OH)_2$ was found to increase at these potentials. While most of these changes occurred near the outer portion of the oxide layer, the Cr_2O_3 barrier layer appeared to be much more resilient, as illustrated by Figs. 9(c) and 10. It did not show any response to the potential changes, in sharp contrast to the hydroxide components. The AES depth profile at a potential of 0.4 V_{SCE} also illustrated some unique features between the first and second passive regions. Upon making the transition from passive I to passive II, the quantity of Ni located on the outer surface decreased dramatically at 0.4 V_{SCE}, only to be replaced by an Fe oxide which was also observed at 0.6 V_{SCE}. Similar results have been observed elsewhere [47]. At 0.75 V_{SCE}, Ni was precipitated back on the outer surface of the oxide film, and the polarisation curve showed nearly an order of magnitude rise in current density between 0.6 and 0.75 V_{SCE}.

The changes that occurred in the structure of the film between the first and second passive regions, and how these changes affected the corrosion resistance can be understood by utilising the impedance data. The significance of Cr in the passivation and protection of Alloy 600 was illustrated in the resistance plots in Fig. 5. When the passive film was formed on the alloy at -0.4 V_{SCE}, the Cr concentration and the resistance of the inner layer increased and remained elevated relative to the pre-passive region. Once the second passive region was entered at 0.4 V_{SCE}, the resistance of the inner layer dropped substantially, as did the Cr content. The resistance of the outer layer, however, began to rise in the second

Table 2
Changes in the oxide film properties determined through the changes in resistance and inverse capacitance.

	Range, V_{SCE}	R_1	$1/C_1$	R_2	$1/C_2$
(1)	-0.6 to 0	Decrease	Increase	Increase	Increase
(2)	0–0.6	Increase	Decrease	Decrease	Decrease

passive region, corresponding to the removal of Ni hydroxide and the subsequent precipitation of Fe oxides on the surface. As long as the Cr barrier layer remained intact, it would continue to provide the majority of protection against corrosion. The impedance data could also provide details on the structural integrity of the oxide film. Changes in the film capacitance can be due to a number of factors, such as a shift in thickness, porosity or composition. The plot in Fig. 6 clearly illustrates these changes as a function of potential. There is a clear division at 0 V_{SCE}, making it difficult to segregate the plot into the pre-passive, passive I and passive II components previously indicated. To simplify the data analysis only two regions were established, using 0 V_{SCE} as the midpoint. The first range (1) contained data from the pre-passive and passive 1 region between -0.6 and 0 V_{SCE}, while the second range (2) contained data from passive 1 and passive 2 regions between 0 and 0.75 V_{SCE}. By tracking both the changes in resistance and inverse capacitance, structural changes in the oxide film can be obtained [25]. The results, shown in Table 2, indicated that in range 1, the decrease in resistance and increase in inverse capacitance resulted from an outer oxide layer that was becoming increasingly porous, while the inner layer in the same range was growing, based on the increase in both inverse capacitance and resistance. In range 2, the outer oxide was becoming more compact, as the resistance increased and the inverse capacitance decreased. The inner layer, however, was beginning to break down, as both the resistance and inverse capacitance values decreased. The inverse capacitance plots showed the largest changes at approximately 0–0.1 V_{SCE}. It was at these same potentials that the resistance plots showed a dramatic change in behaviour. As the potential increased, the outer oxide film transitioned from porous to increasingly compact and more protective as the Fe content increased. The inner layer, on the other hand, transitioned from a strong, compact layer to an increasingly thin and weaker layer.

4. Conclusions

It was determined that the passive film formed on Alloy 600 in 0.1 M $Na_2S_2O_3$ solution was a bilayer oxide film containing a Cr-rich inner layer and a mixed Ni and Fe outer layer, whose growth and breakdown could be explained using the point defect model. The formation of the passive film at -0.4 V_{SCE} was marked by an increase in Cr_2O_3. This component of the oxide film proved to be the most stable, as concentrations did not alter significantly at different applied potentials. The composition of the outer layer was found to be highly dependent upon the applied potential. The oxide film in the pre-passive and first passive region contained mostly Ni hydroxide on the outer surface. The precipitation of Fe oxide on the outer oxide occurred within the second passive region, between 0.4 and 0.6 V_{SCE}. At 0.75 V_{SCE} the Ni hydroxide was again found on the outer surface with Fe oxide buried beneath it. Two anodic peaks were observed at 0.1 and 0.75 V_{SCE}. Due to the rise in current density at these potentials, it was believed that film breakdown had occurred. At both of these potentials a spike in $Ni(OH)_2$ was observed while a decrease in $Cr(OH)_3$ was seen only at 0.1 V_{SCE}, since the outer Cr content was already depleted upon entering the second passive region. Corrosion resistance was dictated by the inner layer at all potentials but was highest in
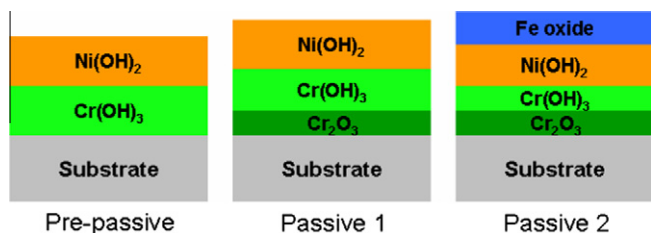

Fig. 15. Layered oxide film on Alloy 600 within the pre-passive (-0.6 to -0.4 V_{SCE}), passive 1 (-0.4 to 0.4 V_{SCE}) and passive 2 (0.4–0.75 V_{SCE}) region.

the passive region before the first anodic peak. The removal of $Cr(OH)_3$ at 0.4 V_{SCE} was met by a drop in protection by the inner layer while the precipitation of Fe increased the resistance of the outer layer. The porosity of the outer layer was always higher when $Ni(OH)_2$ was the predominant species on the outer layer.

Acknowledgements

References

[1] Russel H. Jones, Stress corrosion cracking: materials performance and evaluation, 1992.
[2] O.S. Tatone, R.S. Pathania, Nucl. Safety 21 (1980) 766–780.
[3] H. Coriou, L. Grall, C. Mahieu, M. Pelas, Corrosion 22 (1966) 280–287.
[4] J.R. Park, Z. Szklarska-Smialowska, Corrosion 41 (1985) 665–675.
[5] V.B. Rajan, G.S. Was, Corrosion 43 (1987) 305–308.
[6] L.A.S. Ries, M. Da Cunha Belo, M.G.S. Ferreira, I.L. Miller, Corros. Sci. 50 (2008) 676–686.
[7] M. Bojinov, G. Fabricius, P. Kinnunen, T. Laitinen, K. Makela, T. Saario, G. Sundholm, K. Yliniemi, Electrochim. Acta 47 (2002) 1697–1712.
[8] J.-J. Park, S.-I. Pyun, S.-B. Lee, Electrochim. Acta 49 (2004) 281–292.
[9] S.-S. Hwang, H.-P. Kim, Y.-S. Lim, J.-S. Kim, L. Thomas, Corros. Sci. 49 (2007) 3797–3811.
[10] W.-T. Tsai, M.-J. Sheu, J.-T. Lee, Corros. Sci. 38 (1996) 33–45.
[11] D.-J. Kim, H.-C. Kwon, H.-P. Kim, Corros. Sci. 50 (2008) 1221–1227.
[12] W.-T. Tsai, C.-H. Chou, Mater. Sci. Eng. A288 (2000) 5–11.
[13] W.-T. Tsai, Z.-H. Lee, J.-T. Lee, M.-C. Tsai, P.-H. Lo, Mater. Sci. Eng. A118 (1989) 121–129.
[14] I.J. Yang, Corrosion 49 (1993) 576–584.
[15] W.-T. Tsai, C.-S. Chang, J.-T. Lee, Corrosion 50 (1994) 98–106.
[16] H.S. Isaacs, B. Vyas, M.W. Kendig, Corrosion 38 (1982) 130–136.
[17] M.-C. Tsai, W.-T. Tsai, J.-T. Lee, Corros. Sci. 34 (1993) 741–757.
[18] W. Yang, Z. Lu, D. Huang, D. Kong, G. Zhao, J. Congleton, Corros. Sci. 43 (2001) 963–977.
[19] J.K. Lee, Z. Szklarska-Smialowska, Corrosion 44 (1987) 560–565.
[20] H.H. Horowitz, J. Electrochem. Soc. 132 (1985) 2063–2071.
[21] M. Da Cunha Belo, N.E. Hakiki, M.G.S. Ferreira, Electrochim. Acta 44 (1999) 2473–2481.
[22] J.R. Macdonald, Impedance Spectroscopy: Emphasizing Solid Materials and Systems, John Wiley & Sons, New York, 1987.
[23] K. Juttner, Electrochim. Acta 35 (1990) 1501–1508.
[24] J.-S. Baek, J.-G. Kim, D.-H. Hur, J.-S. Kim, Corros. Sci. 45 (2003) 983–994.
[25] J.J. Gray, C.A. Orme, Electrochim. Acta 52 (2007) 2370–2375.
[26] V. Mei-Wen Huang, V. Vivier, M.E. Orazem, N. Pebere, B. Tribollet, J. Electrochem. Soc. 154 (2007) C99–C107.
[27] C.H. Hsu, F. Mansfeld, Corrosion 57 (2001) 747–748.
[28] M. Seo, N. Sato, Corrosion 36 (1980) 334–339.
[29] L. Zhang, D.D. Macdonald, Electrochim. Acta 43 (1998) 2661–2671.
[30] A.S. Lim, A. Atrens, Appl. Phys. A 54 (1992) 343–349.
[31] S. Mischler, A. Vogel, H.J. Mathieu, D. Landolt, Corros. Sci. 32 (1991) 925–944.
[32] E. Sikora, D. Macdonald, Electrochim. Acta 48 (2002) 69–77.
[33] A.C. Lloyd, D.W. Shoesmith, N.S. McIntyre, J.J. Noel, J. Electrochem. Soc. 150 (2003) B120–B130.
[34] D. Marijan, M. Vukovic, J. Appl. Electrochem. 28 (1998) 96–102.
[35] D.D. Macdonald, A. Sun, Electrochim. Acta 51 (2006) 1767–1779.
[36] J. Robertson, Corros. Sci. 32 (1991) 443–463.
[37] M.C. Biesinger, C. Brown, J.R. Mycroft, R.D. Davidson, N.S. McIntyre, Surf. Interface Anal. 36 (2004) 1550–1563.
[38] P. Keller, H.-H. Strehblow, Corros. Sci. 46 (2004) 1939–1952.
[39] M.C. Biesinger, B.P. Payne, L.W.M. Lau, A. Gerson, R. Smart, Surf. Interface Anal. 41 (2009) 324–332.
[40] V. Maurice, W.P. Yang, P. Marcus, J. Electrochem. Soc. 145 (1998) 909–919.
[41] C.D. Wagner, A.V. Naumkin, A. Kraut-Vass, J.W. Allison, C.J. Powell, J.R. Rumble Jr., NIST Standard Reference Database 20, Version 3.5 (web version). <http://srdata.nist.gov/xps/>, 2007.
[42] C.Y. Chao, L.F. Lin, D.D. Macdonald, J. Electrochem. Soc. 128 (1981) 1187–1193.
[43] L.F. Lin, C.Y. Chao, D.D. Macdonald, J. Electrochem. Soc. 128 (1981) 1194–1198.
[44] C.Y. Chao, L.F. Lin, D.D. Macdonald, J. Electrochem. Soc. 129 (1982) 1874–1879.
[45] L.G. McMillion, A. Sun, D.D. Macdonald, D.A. Jones, Metal. Trans. A 36A (2005) 1129–1141.
[46] A. Machet, A. Galtayries, S. Zanna, L. Klein, V. Maurice, P. Jolivet, M. Foucault, P. Combrade, P. Scott, P. Marcus, Electrochim. Acta 49 (2004) 3957–3964.
[47] N.S. McIntyre, D.G. Zetaruk, D. Owen, Appl. Surf. Sci. 2 (1978) 55–73.